






Spectral correlation in MODIS water-leaving reflectance retrieval uncertainty

MINWEI ZHANG,^{1,2,*}  AMIR IBRAHIM,²  BRYAN A. FRANZ,²
ANDREW M. SAYER,^{2,3} P. JEREMY WERDELL,²
AND LACHLAN I. MCKINNA^{2,4} 

¹Science Application International Corp., McLean, VA, USA

²Ocean Ecology Laboratory, Goddard Space Flight Center, National Aeronautics and Space Administration, Greenbelt, MD, USA

³GESTAR II, University of Maryland Baltimore County, Baltimore, MD, USA

⁴Go2Q Pty Ltd., Buderim, QLD, Australia

*minwei.zhang@nasa.gov

Abstract: Spectral remote sensing reflectance, $R_{rs}(\lambda)$ (sr^{-1}), is the fundamental quantity used to derive a host of bio-optical and biogeochemical properties of the water column from satellite ocean color measurements. Estimation of uncertainty in those derived geophysical products is therefore dependent on knowledge of the uncertainty in satellite-retrieved R_{rs} . Furthermore, since the associated algorithms require R_{rs} at multiple spectral bands, the spectral (i.e., band-to-band) error covariance in R_{rs} is needed to accurately estimate the uncertainty in those derived properties. This study establishes a derivative-based approach for propagating instrument random noise, instrument systematic uncertainty, and forward model uncertainty into R_{rs} , as retrieved using NASA's multiple-scattering epsilon (MSEPS) atmospheric correction algorithm, to generate pixel-level error covariance in R_{rs} . The approach is applied to measurements from Moderate Resolution Imaging Spectroradiometer (MODIS) on the Aqua satellite and verified using Monte Carlo (MC) analysis. We also make use of this full spectral error covariance in R_{rs} to calculate uncertainty in phytoplankton pigment chlorophyll-a concentration (chl_a , mg/m^3) and diffuse attenuation coefficient of downwelling irradiance at 490 nm ($K_d(490)$, m^{-1}). Accounting for the error covariance in R_{rs} generally reduces the estimated relative uncertainty in chl_a by ~1-2% (absolute value) in waters with $\text{chl}_a < 0.25 \text{ mg}/\text{m}^3$ where the color index (CI) algorithm is used. The reduction is ~5-10% in waters with $\text{chl}_a > 0.35 \text{ mg}/\text{m}^3$ where the blue-green ratio (OCX) algorithm is used. Such reduction can be higher than 30% in some regions. For $K_d(490)$, the reduction by error covariance is generally ~2%, but can be higher than 20% in some regions. The error covariance in R_{rs} is further verified through forward-calculating chl_a from MODIS-retrieved and in situ R_{rs} and comparing estimated uncertainty with observed differences. An 8-day global composite of propagated uncertainty shows that the goal of 35% uncertainty in chl_a can be achieved over deep ocean waters ($\text{chl}_a \leq 0.1 \text{ mg}/\text{m}^3$). While the derivative-based approach generates reasonable error covariance in R_{rs} , some assumptions should be updated as our knowledge improves. These include the inter-band error correlation in top-of-atmosphere reflectance, and uncertainties in the calibration of MODIS 869 nm band, in ancillary data, and in the in situ data used for system vicarious calibration.

© 2024 Optica Publishing Group under the terms of the [Optica Open Access Publishing Agreement](#)

1. Introduction

While ocean color products have been widely used to monitor ocean environments and study global change [1,2], they are generally distributed without detailed estimates of uncertainty (e.g., the products distributed by NASA's Ocean Biology Distributed Active Archive Center (OB.DAAC)). Those products are incomplete without accurate uncertainty estimates, as it limits our ability to interpret small changes observed in aquatic biogeochemical properties. Consequently, the Group

on Earth Observations (GEO) and International Ocean-Colour Coordinating Group (IOCCG) recommend uncertainty provision within the framework of quality assurance for earth observation [3,4].

Historically, the ocean color community has relied on validation (i.e., comparison with collocated in situ data) to estimate uncertainty in ocean color products. While such validation generates reasonable confidence in those products, it has some limitations [5]. Given these limitations, in recent years efforts have been made towards calculating pixel-level uncertainty in remote sensing reflectance ($R_{rs}(\lambda)$, sr^{-1}). This is a key first step, as R_{rs} is the fundamental ocean color product from which a host of bio-optical and biogeochemical properties of the water column can be derived. Bayesian inversion is used to quantify uncertainty in R_{rs} retrieved from Ocean Color—Simultaneous Marine and Aerosol Retrieval Tool (OC-SMART) [6]. An ensemble of artificial neural networks is developed for the atmospheric correction over coastal waters, along with the pixel-level uncertainty in R_{rs} [7]. The European Space Agency's Ocean Color Climate Change Initiative program (OC-CCI) provides pixel-level uncertainty in Level-3 R_{rs} from MEdium Resolution Imaging Spectrometer (MERIS), Sea-viewing Wide Field-of-view Sensor (SeaWiFS), Moderate Resolution Imaging Spectroradiometer (MODIS), Visible Infrared Imaging Radiometer Suite (VIIRS), and Ocean and Land Colour Instrument (OLCI) data [8]. This is done by associating each in situ validation match-up to a specific water type based on spectral classification (optical water type, OWT), using that same classification scheme to assign each satellite R_{rs} retrieval with a set of OWT weights and then computing a weighted average of the validation-based match-up uncertainties to estimate pixel-level uncertainties. As the uncertainty of each OWT is derived from validation against in situ data and OWT alone is not the sole predictor of uncertainty in R_{rs} (as factors such as radiant-path geometry and aerosol loading can strongly influence the uncertainty in satellite retrievals), this approach still suffers from the same validation match-up limitations.

Uncertainty in R_{rs} associated with random effects has also been produced through comparing coincident daily R_{rs} from two satellite missions, or matching satellite retrieved and in situ R_{rs} (i.e., validation) [9], and R_{rs} uncertainty has been estimated by comparing with “ground truth” R_{rs} determined from a phytoplankton pigment chlorophyll-a (chl_a , mg/m^3) algorithm [10]. As the atmospheric correction (AC) algorithms used by those studies are based on Gordon and Wang (1994) (hereafter GW94) [11], which uses two near-infrared bands (NIR) to calculate the aerosol reflectance at visible bands, uncertainty in R_{rs} is inherently spectrally dependent, which means that a spectral (i.e., band-to-band) error covariance exists in R_{rs} .

While error variance (square of standard deviation) in R_{rs} has been estimated in previous studies, few studies have estimated the error covariance. One example that did is [12], where the partial derivative of R_{rs} with respect to top-of-atmosphere (TOA) radiance ($L_t(\lambda)$, $\text{mW}\cdot\text{cm}^{-2}\cdot\mu\text{m}^{-1}\cdot\text{sr}^{-1}$) was numerically approximated. That study considered only a radiometric uncertainty of 0.5% in L_t and neglected other uncertainty sources (e.g., systematic uncertainty, forward model uncertainty) that are known to be relevant [5]. A derivative approach was established to calculate the error covariance in R_{rs} [13] retrieved from Ocean and Land Colour Instrument (OLCI) onboard Sentinel-3 using an AC algorithm for clear water [14], although they also only included sensor noise.

Although error covariance in R_{rs} is known to be important to uncertainty estimates in ocean bio-optical and biogeochemical products [12,13], there is no operational uncertainty product including this spectral error covariance yet, which is why it has been neglected when estimating uncertainty in chl_a [15]. Neither error variance nor covariance in R_{rs} are considered when calculating the uncertainty in inherent optical properties (IOPs) [16]. There is therefore a need for an operational R_{rs} error covariance product for calculating the uncertainty in ocean color products that are derived from bio-optical models using spectral R_{rs} , e.g., blue-green ratio (OCX) [17] or color index (CI) model for chl_a [18], and diffuse attenuation coefficient of downwelling

irradiance at 490 nm ($K_d(490)$, m^{-1}) [19]. Note that the OC-CCI program only provides root mean square difference of R_{rs} but not error covariance.

The Ocean Biology Processing Group (OBPG) at NASA has been distributing global ocean color products for more than two decades. While those products have been used widely, pixel-level uncertainties in R_{rs} have not yet been provided. The OBPG has recently completed a multi-mission ocean color reprocessing using the Multiple-Scattering EPSilon AC algorithm (MSEPS) [20], which has been shown to perform better than GW94 [21]. Since pixel-level error variance in R_{rs} retrieved from MSEPS has been generated by [5], this study will generate the error covariance in R_{rs} using the same propagation method as that presented in [5]. By propagating instrument random noise, instrument systematic uncertainty, and forward model uncertainty through MSEPS, error covariance is generated for R_{rs} retrieved from MODIS, with the goal of establishing a framework for computationally efficient generation of pixel-level error covariance in R_{rs} that can be applied for all ocean color missions processed and distributed by NASA. This study is organized as follows. Satellite data and in situ data used in this study are described in Section 2, followed by a brief description of the MSEPS algorithm and uncertainty propagation through the AC procedure to calculate error covariance in R_{rs} . Two approaches are introduced in Section 2 to evaluate the error covariance in R_{rs} ; one through Monte Carlo and the other through closure analysis with results derived from evaluation of MODIS retrieved chl_a against chl_a calculated using in situ R_{rs} . Section 3 presents the results from the evaluation of error covariance in R_{rs} using these analyses, the evaluation of the effect from error covariance in R_{rs} on uncertainty in chl_a and $K_d(490)$, spectral correlation of the error covariance in R_{rs} , as well as a global 8-day error covariance products. Conclusions are provided in Section 4.

2. Data and methodology

2.1. MODIS data

Using the SeaDAS software package [22] and latest instrument calibration coefficients, as distributed by OB.DAAC [23], calibrated and geolocated (Level-1B) data are generated from uncalibrated (Level-1A) data from MODIS aboard the Aqua satellite, which were also downloaded from OB.DAAC. MODIS data used in this study includes the data over South Pacific Ocean on Apr. 19, 2017, over North America's east coast on Oct. 2, 2013, global data from Dec. 3-10, 2019, and scenes that are matched with in situ data over the Marine Optical Buoy (MOBY) [24] during 2002-2019.

2.2. In situ data

Using the OB.DAAC's in situ data archive and validation search utility tool (SeaBASS, [25]), coincident matchups spanning the years 2002-2019 were collected between MODIS-Aqua retrieved and in situ R_{rs} from MOBY. Chlorophyll-a concentration are calculated from in situ R_{rs} using NASA's standard algorithm, which combines the OCX band-ratio algorithm [17] with the CI band-difference algorithm [18]. Such calculated chl_a is used to evaluate MODIS retrieved chl_a , with the results applied to verify the error covariance in R_{rs} .

2.3. MSEPS atmospheric correction

The purpose of AC is to retrieve water-leaving radiance, $L_w(\lambda)$ ($\text{mW}\cdot\text{cm}^{-2}\cdot\mu\text{m}^{-1}\cdot\text{sr}^{-1}$), from $L_t(\lambda)$, which can be expressed as:

$$L_t/t_g = L_r + L_a + t_{vr}L_f + TL_g + t_vL_w \quad (1)$$

where $t_g(\lambda)$ is two-way gas transmittance, $L_r(\lambda)$ ($\text{mW}\cdot\text{cm}^{-2}\cdot\mu\text{m}^{-1}\cdot\text{sr}^{-1}$) is the radiance from scattering by air molecules in the absence of aerosol, $L_a(\lambda)$ ($\text{mW}\cdot\text{cm}^{-2}\cdot\mu\text{m}^{-1}\cdot\text{sr}^{-1}$) is the radiance from scattering by aerosols that also accounts for interactions between air molecules and aerosol

scattering, $L_f(\lambda)$ ($\text{mW}\cdot\text{cm}^{-2}\cdot\mu\text{m}^{-1}\cdot\text{sr}^{-1}$) is the radiance from scattering by surface whitecaps, $L_g(\lambda)$ ($\text{mW}\cdot\text{cm}^{-2}\cdot\mu\text{m}^{-1}\cdot\text{sr}^{-1}$) is sun glint, $t_{\text{vr}}(\lambda)$ and $t_{\text{v}}(\lambda)$ are the diffuse transmittance from surface to sensor with the former only including molecular scattering and the latter including molecular and aerosol scattering. $T(\lambda)$ is the beam transmittance for view path. As the composition of air molecules is known and stable, L_r can be calculated using vector radiative transfer that accounts for polarization, multiple scattering, and sea state to an uncertainty within 0.1% [26]. L_f is calculated using wind speed based on an empirical model [27,28]. A sun glint coefficient is calculated using a statistical model [29], from which L_g can be derived [30]. The calculation of L_a is detailed by [5,21]. Please note that L_t is corrected for the polarization effects following the approach presented by [31], which has an estimated residual uncertainty of 0.1%. After removing L_r , L_a , L_f , and TL_g from L_t , L_w can be derived and R_{rs} is then calculated by normalizing L_w to downwelling irradiance:

$$R_{\text{rs}} = (L_t/t_g - L_r - TL_g - t_{\text{vr}}L_f - L_a)f_b/(t_{\text{v}}F_0t_s\cos(\theta_s)) \quad (2)$$

where $f_b(\lambda)$ is bidirectional reflectance correction calculated from the model presented by [32] using chl_a , $t_s(\lambda)$ is diffuse transmittance from Sun to surface, θ_s is solar zenith angle, and $F_0(\lambda)$ ($\text{mW}\cdot\text{cm}^{-2}\cdot\mu\text{m}^{-1}$) is extraterrestrial solar irradiance corrected for earth-Sun distance.

2.4. Uncertainty propagation into R_{rs}

To calculate error covariance in R_{rs} using the derivative approach, the partial derivative of R_{rs} with respect to the relevant variables and the uncertainty in those variables are needed. These are the same as for the calculation of error variance in R_{rs} presented by [5]. The difference between error variance and covariance is the equations used to calculate them based on the partial derivative of R_{rs} and uncertainty in uncertainty variables. In this section, we briefly recap the uncertainty sources and propagation approach detailed in [5], and then describe the approach that are used to calculate the error covariance in R_{rs} .

The uncertainty sources for R_{rs} are categorized into three types:

- (1) Instrument random noise;
- (2) Instrument systematic uncertainty;
- (3) Forward model uncertainty, including contributions from the models for L_r , L_a , L_f , L_g , f_b , and L_w , and uncertainty in ancillary data inputs to those models.

In general, for two variables y_1 and y_2 that are a function of variables x , z expressed as:

$$\begin{cases} y_1 = f_1(x_1, x_2, \dots, x_n) \\ y_2 = f_2(z_1, z_2, \dots, z_n) \end{cases} \quad (3)$$

error covariance between y_1 and y_2 , denoted by $u(y_1, y_2)$ [33], can be calculated from:

$$u(y_1, y_2) = \left(\frac{\partial f_1}{\partial x_1}, \frac{\partial f_1}{\partial x_2}, \dots, \frac{\partial f_1}{\partial x_n} \right) \begin{bmatrix} u(x_1, z_1) & \dots & u(x_1, z_n) \\ \vdots & \ddots & \vdots \\ u(x_n, z_1) & \dots & u(x_n, z_n) \end{bmatrix} \left(\frac{\partial f_2}{\partial z_1}, \frac{\partial f_2}{\partial z_2}, \dots, \frac{\partial f_2}{\partial z_n} \right)^T \quad (4)$$

where $u(x_i, z_j)$ represents the error covariance between variables x_i and z_j , $\frac{\partial f_1}{\partial x_i}$ and $\frac{\partial f_2}{\partial z_j}$ are the partial derivative of y_1 with respect to x_i and of y_2 with respect to z_j , T is the transpose operator. Please note that Eq. (4) can also be used to calculate error variance of y_1 , denoted by $u^2(y_1)$, when $f_2 = f_1$ and variable z is the same as x .

Based on Eq. (4) to calculate error covariance between $R_{rs}(\lambda_i)$ and $R_{rs}(\lambda_j)$, denoted by $u(R_{rs}(\lambda_i), R_{rs}(\lambda_j))$, the variables contributing to uncertainty in $R_{rs}(\lambda_i)$ and $R_{rs}(\lambda_j)$ need to be identified. Note that when $\lambda_i = \lambda_j$, error covariance becomes error variance, denoted by $u^2(R_{rs}(\lambda_i))$ for simplicity. A vector for uncertainty variables for $R_{rs}(\lambda_i)$ is defined as:

$$X_i = [L_{\text{rfc}}(\lambda_i), L_{\text{rfc}}(\text{NIR}), \text{chl}_a, \tau'_a(869), rh] \quad (5)$$

where L_{rfc} is:

$$L_{\text{rfc}} = L_t/t_g - L_r - t_{\text{vr}}L_f \quad (6)$$

Combining Eqs. (4) and (5), $u(R_{rs}(\lambda_i), R_{rs}(\lambda_j))$ can be calculated as:

$$u(R_{rs}(\lambda_i), R_{rs}(\lambda_j)) = \frac{\partial R_{rs}(\lambda_i)}{\partial X_i} C_{R_{rs}} \left(\frac{\partial R_{rs}(\lambda_j)}{\partial X_j} \right)^T \quad (7a)$$

where

$$\frac{\partial R_{rs}(\lambda_i)}{\partial X_i} = \left(\frac{\partial R_{rs}(\lambda_i)}{\partial L_{\text{rfc}}(\lambda_i)}, \frac{\partial R_{rs}(\lambda_i)}{\partial L_{\text{rfc}}(\text{NIR})}, \frac{\partial R_{rs}(\lambda_i)}{\partial \text{chl}_a}, \frac{\partial R_{rs}(\lambda_i)}{\partial \tau'_a(869)}, \frac{\partial R_{rs}(\lambda_i)}{\partial rh} \right) \quad (7b)$$

$$C_{R_{rs}} = \begin{bmatrix} u(L_{\text{rfc}}(\lambda_i), L_{\text{rfc}}(\lambda_j)) & u(L_{\text{rfc}}(\lambda_i), L_{\text{rfc}}(\text{NIR})) & 0 & 0 & 0 \\ u(L_{\text{rfc}}(\text{NIR}), L_{\text{rfc}}(\lambda_j)) & u^2(L_{\text{rfc}}(\text{NIR})) & 0 & 0 & 0 \\ 0 & 0 & u^2(\text{chl}_a) & 0 & 0 \\ 0 & 0 & 0 & u^2(\tau'_a(869)) & 0 \\ 0 & 0 & 0 & 0 & u^2(rh) \end{bmatrix} \quad (7c)$$

While calculation of $\frac{\partial R_{rs}(\lambda)}{\partial X}$ is detailed by [5], $C_{R_{rs}}$ is quantified as follows.

(1) $u(L_{\text{rfc}}(\lambda_i), L_{\text{rfc}}(\lambda_j))$. $u(L_{\text{rfc}}(\lambda_i), L_{\text{rfc}}(\lambda_j))$ is calculated similarly to $u(R_{rs}(\lambda_i), R_{rs}(\lambda_j))$ but with X_i expressed as follows:

$$X_i = [L_t(\lambda_i), t_g(\lambda_i), L_r(\lambda_i), t_{\text{vr}}(\lambda_i), L_f(\lambda_i)] \quad (8)$$

$u(L_{\text{rfc}}(\lambda_i), L_{\text{rfc}}(\lambda_j))$ is derived from:

$$u(L_{\text{rfc}}(\lambda_i), L_{\text{rfc}}(\lambda_j)) = \frac{\partial L_{\text{rfc}}(\lambda_i)}{\partial X_i} C_{L_{\text{rfc}}} \left(\frac{\partial L_{\text{rfc}}(\lambda_j)}{\partial X_j} \right)^T \quad (9a)$$

where

$$\frac{\partial L_{\text{rfc}}(\lambda_i)}{\partial X_i} = \left(\frac{\partial L_{\text{rfc}}(\lambda_i)}{\partial L_t(\lambda_i)}, \frac{\partial L_{\text{rfc}}(\lambda_i)}{\partial t_g(\lambda_i)}, \frac{\partial L_{\text{rfc}}(\lambda_i)}{\partial L_r(\lambda_i)}, \frac{\partial L_{\text{rfc}}(\lambda_i)}{\partial t_{\text{vr}}(\lambda_i)}, \frac{\partial L_{\text{rfc}}(\lambda_i)}{\partial L_f(\lambda_i)} \right) \quad (9b)$$

$$C_{L_{\text{rfc}}} = \begin{bmatrix} u(L_t(\lambda_i), L_t(\lambda_j)) & 0 & 0 & 0 & 0 \\ 0 & u(t_g(\lambda_i), t_g(\lambda_j)) & 0 & 0 & 0 \\ 0 & 0 & u(L_r(\lambda_i), L_r(\lambda_j)) & u(L_r(\lambda_i), t_{\text{vr}}(\lambda_j)) & u(L_r(\lambda_i), L_f(\lambda_j)) \\ 0 & 0 & u(t_{\text{vr}}(\lambda_i), L_r(\lambda_j)) & u(t_{\text{vr}}(\lambda_i), t_{\text{vr}}(\lambda_j)) & 0 \\ 0 & 0 & u(L_f(\lambda_i), L_r(\lambda_j)) & 0 & u(L_f(\lambda_i), L_r(\lambda_j)) \end{bmatrix} \quad (9c)$$

$\frac{\partial L_{\text{rfc}}(\lambda_i)}{\partial X_i}$ and $\frac{\partial L_{\text{rfc}}(\lambda_j)}{\partial X_j}$ can be calculated based on Eq. (6). For the elements of Eq. (9c), $u(L_t(\lambda_i), L_t(\lambda_j))$ is derived from:

$$u(L_t(\lambda_i), L_t(\lambda_j)) = r(\rho_t(\lambda_i), \rho_t(\lambda_j)) u(L_t(\lambda_i)) u(L_t(\lambda_j)) \quad (10)$$

where $u(L_t)$ is the product of L_t and the sum of systematic uncertainty and forward model uncertainty, which are derived from the system vicarious calibration assuming a 2% calibration

uncertainty at 869-nm band and a 2.3%-4.4% uncertainty in the blue-red wavelengths for in situ L_w at MOBY, which are estimated using upwelling radiance ($L_u(\lambda)$, $\text{mW}\cdot\text{cm}^{-2}\cdot\mu\text{m}^{-1}\cdot\text{sr}^{-1}$) uncertainty presented by [34] and the environmental uncertainty (personal communication with Kenneth J Voss). Readers are referred to [5] for the detailed quantification of those two uncertainty sources. The parameter r is the band-to-band correlations in uncertainty in TOA reflectance (ρ_t). This is detailed in Appendix C of [5], with the values for MODIS listed in Table 1; a limitation is that this was calculated as a spectral correlation in TOA reflectance, and it is assumed that these correlation coefficients also hold for TOA reflectance uncertainty. The form of Eq. (10), however, holds regardless of the calculation of r . Based on Eq. (11), $u(t_g(\lambda_i), t_g(\lambda_j))$ can be derived.

$$u(t_g(\lambda_i), t_g(\lambda_j)) = \sum_{k=1}^n \frac{\partial t_g(\lambda_i)}{\partial M_k} \frac{\partial t_g(\lambda_j)}{\partial M_k} u^2(M_k) \quad (11)$$

where M_k is concentration of gas species k ($n = 3$ species: ozone(oz), water vapor (wv), nitrogen dioxide (NO_2)). $\frac{\partial t_g}{\partial M}$ is derived from the model to calculate the transmittance for a specific gas. $u(M_k)$ is the standard uncertainty in gas concentration from local temporal variability, taken as the difference between the two temporal samples that bound the time of satellite observation. A similar approach is used to calculate other components of Eq. (9c). Note that uncertainty in L_r results from uncertainty in wind speed (ws) and surface pressure (pr). Uncertainty in t_{τ} results from uncertainty in pr . Uncertainty in L_f results from uncertainty in ws .

(2) $u(\tau'_a(869))$ and $u(chl_a)$. For the first iteration that is used to account for the non-zero $L_w(\text{NIR})$, $\tau'_a(869)$ and chl_a are assumed constant with zero uncertainty. For the i^{th} iteration, $u(\tau_a(869))$ is derived from:

$$u^2(\tau_a(869)) = \sum_{i=1}^5 \left(\frac{\partial \tau_a(869)}{\partial x_i} \right)^2 u^2(x_i) + 2 \sum_{i=1}^4 \sum_{j=i+1}^5 \frac{\partial \tau_a(869)}{\partial x_i} \frac{\partial \tau_a(869)}{\partial x_j} u(x_i, x_j) \quad (12)$$

where x_i are the elements of the vector in Eq.(5) but replacing λ_i with the 869 nm band. $u^2(chl_a)$ is derived from:

$$u^2(chl_a) = \sum_{i=1}^4 \left(\frac{\partial chl_a}{\partial R_{rs}(\lambda_i)} \right)^2 u^2(R_{rs}(\lambda_i)) + 2 \sum_{i=1}^3 \sum_{j=i+1}^4 \frac{\partial chl_a}{\partial R_{rs}(\lambda_i)} \frac{\partial chl_a}{\partial R_{rs}(\lambda_j)} u(R_{rs}(\lambda_i), R_{rs}(\lambda_j)) + u_m^2 \quad (13)$$

where λ includes bands at 443, 488, 547, and 667 nm for NASA's standard algorithm. $u(R_{rs}(\lambda_i), R_{rs}(\lambda_j))$ is from each iteration. u_m is the model fitting uncertainty, calculated from multiplying the mean relative uncertainty by chl_a . The mean relative uncertainty of 13% is derived by averaging the relative difference between model fitted and in situ chl_a over all the data points that are used to fit the model coefficients in [18], although it is worth noting that the relative uncertainty is for the CI algorithm and may not be applicable to OCX. $u(chl_a)$ and $u(\tau_a(869))$ derived from the i^{th} iteration are used for the $(i+1)^{\text{th}}$ iteration.

(3) $u(rh)$. This is calculated as the local temporal variability, i.e., difference between the two temporal samples that bound the time of satellite observation.

2.5. Verification of error covariance using Monte Carlo analysis

$u(R_{rs}(\lambda_i), R_{rs}(\lambda_j))$ from the derivative approach is verified using Monte Carlo analysis when all uncertainty sources are included. A Gaussian random noise is generated to represent the instrument random noise:

$$L_{\text{noise}} = G\left(0, \frac{\chi}{L_t}\right) L_t \quad (14a)$$

where χ is sensor noise calculated using the model described by [5], $G\left(0, \frac{\chi}{L_t}\right)$ is a random number generated based on a Gaussian distribution with mean of 0 and standard deviation of $\frac{\chi}{L_t}$.

As the systematic and forward model uncertainty are spectrally dependent, the correlated random uncertainty at those 12 bands in Table 1 is generated from:

$$L_{\text{sys+model}} = L G(0, 1) \quad (14b)$$

where $L_{12 \times 12}$ represents the lower triangular matrix derived from the Cholesky decomposition of error covariance matrix of L_t , $u(L_t(\lambda_i), L_t(\lambda_j))$ calculated from Eq. (10) [35]. $G(0,1)_{12 \times 1}$ is the random number generated based on a Gaussian distribution with mean of 0 and standard deviation of 1. This preserves the spectral structure of the correlation in systematic and forward model uncertainty. L_{noise} and $L_{\text{sys+model}}$ are added to L_t , providing L'_t :

$$L'_t = L_t + L_{\text{noise}} + L_{\text{sys+model}} \quad (15)$$

MSEPS is applied to L'_t with the resulting R_{rs} denoted by R'_{rs} . If a total of N (in this study, 2000) samples of R'_{rs} are generated, the error covariance between R_{rs} at bands λ_i and λ_j can be derived from:

$$u(R_{\text{rs}}(\lambda_i), R_{\text{rs}}(\lambda_j)) = \frac{\sum_{n=1}^N (R'_{\text{rsn}}(\lambda_i) - R_{\text{rs}}(\lambda_i))(R'_{\text{rsn}}(\lambda_j) - R_{\text{rs}}(\lambda_j))}{N} \quad (16)$$

where R'_{rsn} represents R_{rs} derived from L'_t . R_{rs} is derived from L_t without sensor noise, systematic and forward model uncertainty.

Table 1. Correlation coefficients (r) between ρ_t .

	412	443	469	488	531	547	555	645	667	678	748
412	1.0										
443	0.88	1.0									
469	0.8	0.87	1.0								
488	0.78	0.88	0.89	1.0							
531	0.66	0.76	0.82	0.91	1.0						
547	0.65	0.75	0.81	0.90	0.96	1.0					
555	0.60	0.70	0.76	0.84	0.88	0.89	1.0				
645	0.53	0.62	0.69	0.77	0.85	0.86	0.8	1.0			
667	0.56	0.65	0.72	0.81	0.90	0.92	0.85	0.89	1.0		
678	0.55	0.65	0.72	0.77	0.90	0.92	0.85	0.9	0.98	1.0	
748	0.51	0.59	0.68	0.74	0.85	0.87	0.81	0.88	0.97	0.97	1.0
869	0.45	0.53	0.63	0.68	0.80	0.82	0.76	0.86	0.94	0.95	0.97

2.6. Verification of error covariance using validation results from chl_a

As R_{rs} at multiple bands is used to calculate chl_a in NASA's standard algorithm, error covariance in R_{rs} between those bands is needed to calculate $u(chl_a)$, and thus can be verified by evaluating $u(chl_a)$. In other words, if the uncertainty in chl_a is reasonable, so is the error covariance in R_{rs} . A similar approach to that used by [36] for evaluating uncertainty in normalized water-leaving radiance and by [37] for evaluating uncertainty in τ_a is used here to evaluate the uncertainty in chl_a . Specifically, an expected discrepancy (Δ_D) between MODIS-retrieved chl_a and chl_a calculated from in situ R_{rs} (named derived chl_a) can be calculated by adding in quadrature the uncertainty in satellite retrieved and derived chl_a and the amount of discrepancy expected due to spatiotemporal variations in the underlying chl_a field (sampling mismatch uncertainty). The

normalized difference Δ_N is defined as the ratio of actual retrieval difference to Δ_D , i.e.,

$$\Delta_N = \frac{chl_a^m - chl_a^d}{\Delta_D} \quad (17)$$

where chl_a^m and chl_a^d represent MODIS retrieved and derived chl_a respectively. If the uncertainties in these quantities and the spatiotemporal mismatch effects are calculated appropriately, and the sample size is sufficient, the ensemble of Δ_N should be close to a Gaussian distribution with mean 0 and variance 1. We can first qualitatively evaluate $u(chl_a)$ by checking the probability density function (PDF) of Δ_N against that of a Gaussian distribution. Taking this a step further, a total of N matchups is divided into n equally populated bins based on Δ_D indexed from low to high. For each bin, the 68th percentile of absolute retrieval difference, which is close to the standard deviation (1σ) for a Gaussian distribution, is plotted against the mean Δ_D . If Δ_D is reasonable, the points should lie along the 1:1 line [37].

3. Results

3.1. Evaluation of $u(R_{rs}(\lambda_i), R_{rs}(\lambda_j))$ against Monte Carlo analysis

$u(R_{rs}(\lambda_i), R_{rs}(\lambda_j))$ from the derivative method is compared with that from MC for a 5-minute MODIS/Aqua granule collected over the South Pacific Ocean (a region of very clear waters, $chl_a < 0.1 \text{ mg/m}^3$) on Apr.19, 2017. We can see from Fig. 1 that the error covariance derived from the two methods show a similar spatial pattern, with values higher at the edge than at the center of the swath. The higher value arises from the high TOA signal due to the longer path length, which leads to higher sensor noise, systematic, and forward model uncertainty [5]. The two compare quantitatively very well, with the median ratio of the derivative method to MC for $u(R_{rs}(443), R_{rs}(547))$ and $u(R_{rs}(443), R_{rs}(667))$ of 0.87 and 1.10, respectively. Considering the negative value of $u(R_{rs}(443), R_{rs}(667))$, a ratio of 1.10 means a smaller numerator than denominator. The PDFs of the ratio shows that $u(R_{rs}(443), R_{rs}(547))$ and $u(R_{rs}(443), R_{rs}(667))$ from the derivative method tend to be underestimated. The underestimation probably results from unknown uncertainty sources, e.g., structured errors [38]. The comparison with MC results demonstrates that the derivative method established to propagate sensor noise, systematic, and forward model uncertainty into R_{rs} is reliable.

3.2. Closure analysis with results from validation against in situ chl_a

As described in section 2.6, uncertainty in derived chl_a is needed for the evaluation of $u(chl_a)$ using results derived from evaluation of MODIS retrieved chl_a against derived chl_a . Uncertainty in R_{rs} at VIS bands of MOBY are approximately 5% [5]. Propagating uncertainty in in situ R_{rs} and the model fitting uncertainty in Eq. (13) gives the uncertainty in derived chl_a . The spatial variation is taken as the standard deviation of MODIS retrieved chl_a over a window of 5×5 pixels centered on the in situ R_{rs} measurement. Figure 2(a) shows the PDF of normalized difference (Δ_N from Eq. (17)) and the theoretical Gaussian distribution. Those two distributions should ideally match if all the uncertainty estimates used to calculate the expected discrepancy (Δ_D) are reliable. 472 matching pairs are used to calculate the PDF. chl_a tends to be biased, with PDF not centered around zero. Figure 2(b) shows binned Δ_D vs. 1σ of the absolute difference between MODIS retrieved and derived chl_a within each bin. Requiring at least 100 matchups per bin for better statistical robustness gives four bins each with 118 matchups here. Overall, Δ_D agrees reasonably well with 1σ points of absolute difference, which shows that error covariance/variance in R_{rs} used to calculate $u(chl_a)$ has skill in distinguishing relatively high-uncertainty cases from low-uncertainty cases. Δ_D tends to be underestimated in low values but overestimated in high values. This could be partly due to the model fitting uncertainty, which is assumed constant at 13%. Ideally, the model fitting uncertainty should be quantified through the uncertainty in fitting

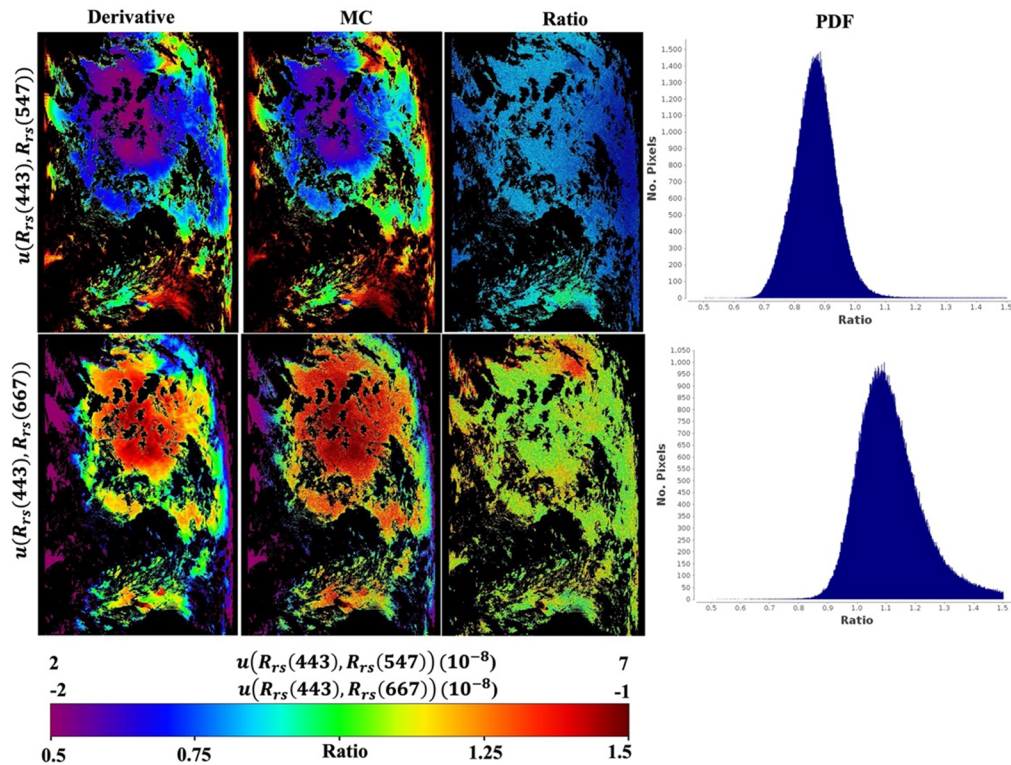


Fig. 1. $u(R_{rs}(443), R_{rs}(547))$ (upper row) and $u(R_{rs}(443), R_{rs}(667))$ (lower row) derived from applying derivative method and MC to MODIS data over South Pacific ocean on Apr. 19, 2017. Instrument random noise, systematic uncertainty, and forward model uncertainty are included. The ratio is calculated from dividing the error covariance from derivative method by that from MC. PDF is for the ratio.

coefficients. That requires the uncertainty in in situ R_{rs} and chl_a that are used to do the fitting, although this is not easy to quantify as the in situ data were collected over 3-4 decades with a variety of instruments and measurement techniques.

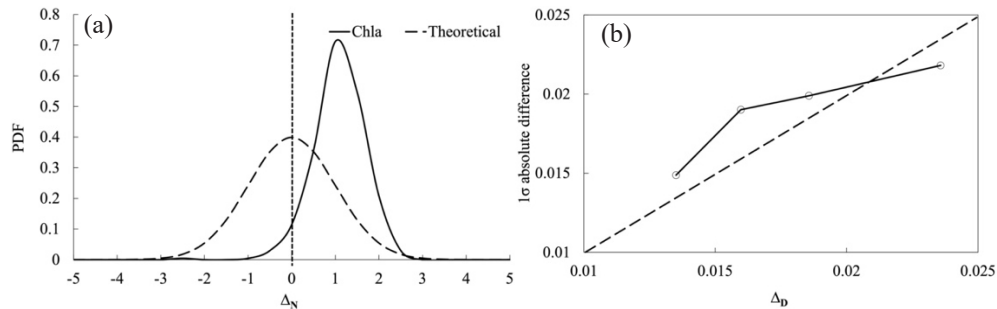


Fig. 2. (a) PDF for the normalized difference (Δ_N) between MODIS retrieved chl_a and chl_a calculated from in situ R_{rs} at MOBY. (b) Expected discrepancy (Δ_D) versus 1σ of absolute difference between MODIS retrieved chl_a and chl_a calculated from in situ R_{rs} at MOBY.

3.3. Effect from error covariance in R_{rs} on uncertainty in chl_a and $K_d(490)$

As spectral R_{rs} is used to calculate chl_a and $K_d(490)$, uncertainty in those products can be used to evaluate error covariance in R_{rs} between those bands. Specifically, $u(R_{rs}(\lambda_i), R_{rs}(\lambda_j))$ is assessed through the spatial variation in relative uncertainty in chl_a , denoted by $\delta(chl_a)$ (i.e., $u(chl_a)*100/chl_a$). chl_a is retrieved using NASA's standard algorithm as described above. Figure 3 shows one example using MODIS data over a transitional zone from turbid ($chl_a > 10 \text{ mg/m}^3$) to clear waters ($chl_a < 0.1 \text{ mg/m}^3$). As $u(R_{rs}(\lambda_i), R_{rs}(\lambda_j))$ has until now been neglected when calculating $u(chl_a)$ [15,16], the effect is evaluated by comparing $\delta(chl_a)$ including $u(R_{rs}(\lambda_i), R_{rs}(\lambda_j))$ with $\delta(chl_a)$ without $u(R_{rs}(\lambda_i), R_{rs}(\lambda_j))$ (see Eq.(13)). While in general the difference derived by subtracting $\delta(chl_a)$ including $u(R_{rs}(\lambda_i), R_{rs}(\lambda_j))$ from that excluding $u(R_{rs}(\lambda_i), R_{rs}(\lambda_j))$ ranges from $\sim 1\text{-}2\%$ in waters with $chl_a < 0.25 \text{ mg/m}^3$ where the CI algorithm is used to $\sim 5\text{-}10\%$ in waters with $chl_a > 0.35 \text{ mg/m}^3$ where the OCX algorithm is used, it can reach $>30\%$ in some regions (Fig. 3(c)). The error covariance reduces $u(chl_a)$ more for OCX than for CI, due to the relatively smaller contribution from model fitting uncertainty in waters where OCX is used, as indicated in Fig. 4.

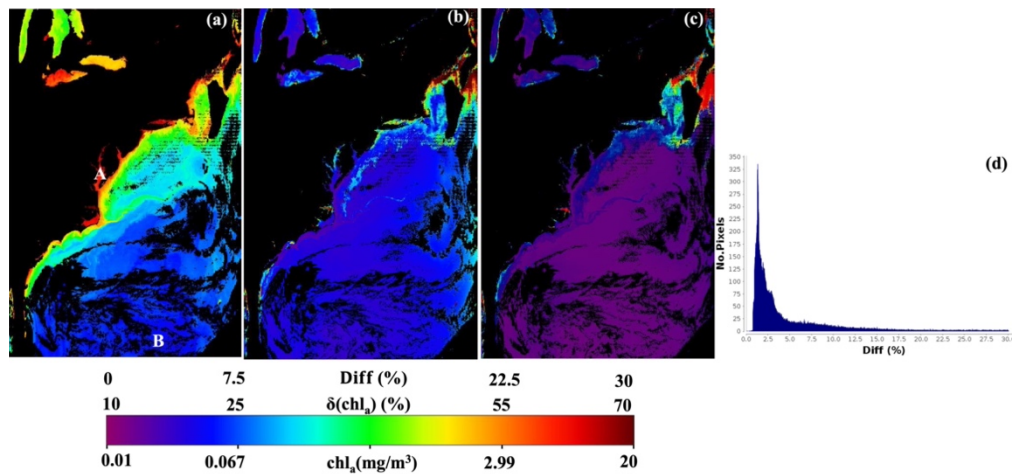


Fig. 3. Uncertainty in chl_a calculated using the error covariance in R_{rs} derived by applying the derivative method to a MODIS scene on Oct. 2, 2013. (a) chl_a , (b) $\delta(chl_a)$ calculated by including error covariance in R_{rs} , (c) the difference derived by subtracting $\delta(chl_a)$ in (b) from that calculated without error covariance in R_{rs} , and (d) PDF of the difference in (c).

The effect of including error covariance in R_{rs} on the uncertainty in $K_d(490)$ is shown in Fig. 5. Here $K_d(490)$ is calculated using NASA's standard algorithm for MODIS [39]. Details of the uncertainty propagation from R_{rs} to $K_d(490)$ are provided by [12]. It should be noted that a relative model fitting uncertainty of 10% is also included in the uncertainty budget of $K_d(490)$. While error covariance in R_{rs} reduces the relative uncertainty in $K_d(490)$ by $\sim 2\%$, it can be $>20\%$ in some regions with smaller contribution of model fitting uncertainty. It should be noted that

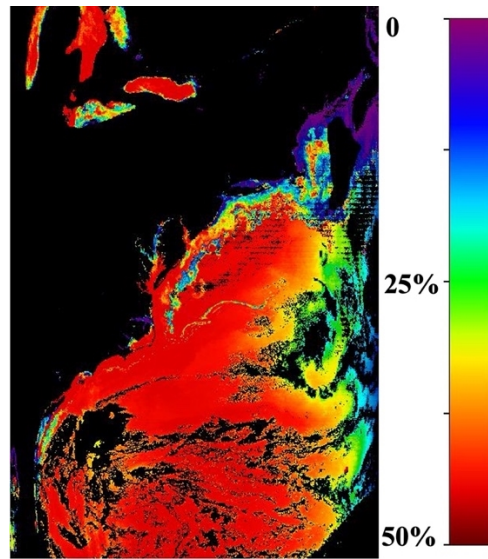


Fig. 4. Ratio between $u^2(\text{chl}_a)$ resulting from model fitting uncertainty only to that from both R_{rs} uncertainty and model fitting uncertainty, for the same MODIS granule as in Fig. 3.

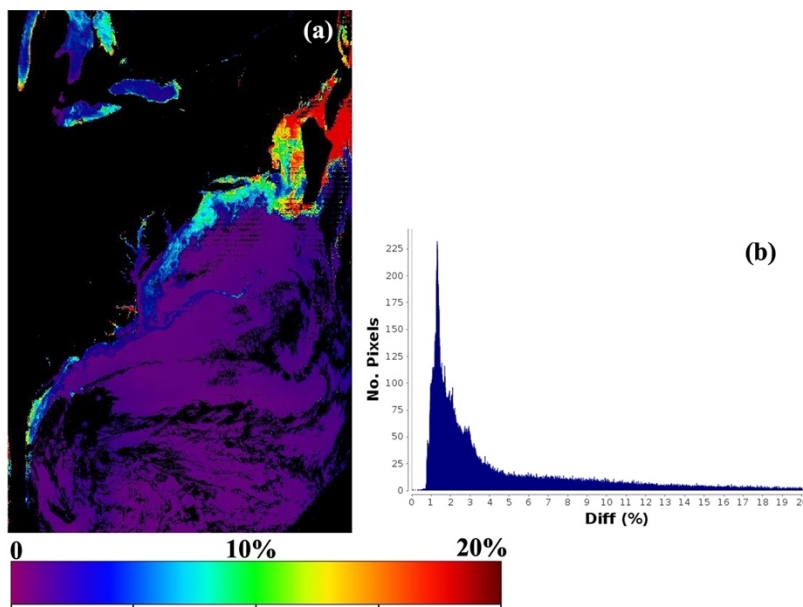


Fig. 5. (a) Difference between relative uncertainty in $K_d(490)$, denoted by $\delta(K_d(490))$, calculated by including $u(R_{rs}(488), R_{rs}(547))$ and that calculated excluding $u(R_{rs}(488), R_{rs}(547))$. (b) PDF of the difference. Data are for the same MODIS granule in Fig. 3.

those numbers of the relative uncertainty in chl_a and $K_d(490)$ reduced by error covariance in R_{rs} is absolute, e.g., 2% in $K_d(490)$ means the relative uncertainty decreases from X% to (X-2)%.

3.4. Examination of pixel-level spectral $r(R_{rs}(\lambda_i), R_{rs}(\lambda_j))$

While $u(R_{rs}(\lambda_i), R_{rs}(\lambda_j))$ is needed for calculating uncertainty in bio-optical and biogeochemical properties, the correlation coefficient between uncertainty in R_{rs} at different bands, denoted by $r(R_{rs}(\lambda_i), R_{rs}(\lambda_j))$, is more directly interpretable. Figure 6 shows two examples of $r(R_{rs}(\lambda_i), R_{rs}(\lambda_j))$ over coastal and open ocean waters. r generally decreases with the increase of wavelength difference between the two bands. This is because the aerosol reflectance is extrapolated from the 869 nm band, which means larger uncertainty at bands farther from 869 nm, and stronger correlation between uncertainty in bands at small wavelength separation. Figure 7 shows the corresponding spectral correlation coefficients $r(R_{rs}(443), R_{rs}(\lambda))$ and $r(R_{rs}(547), R_{rs}(\lambda))$. $r(R_{rs}(443), R_{rs}(\text{blue}))$ and $r(R_{rs}(443), R_{rs}(\text{red}))$ are higher in open ocean waters than that in coastal waters. The higher correlation is probably due to the simplicity of water optical properties in open ocean, dominated by phytoplankton, which affects R_{rs} in blue and red wavelengths in a similar way. $r(R_{rs}(547), R_{rs}(\lambda))$ is lower in open ocean waters than that in coastal waters, due to the small variation of $R_{rs}(547)$ with phytoplankton in open ocean waters. $r(R_{rs}(547), R_{rs}(\text{NIR}))$, $r(R_{rs}(443), R_{rs}(\text{NIR}))$ and $r(R_{rs}(547), R_{rs}(\text{red}))$ are close to 0.

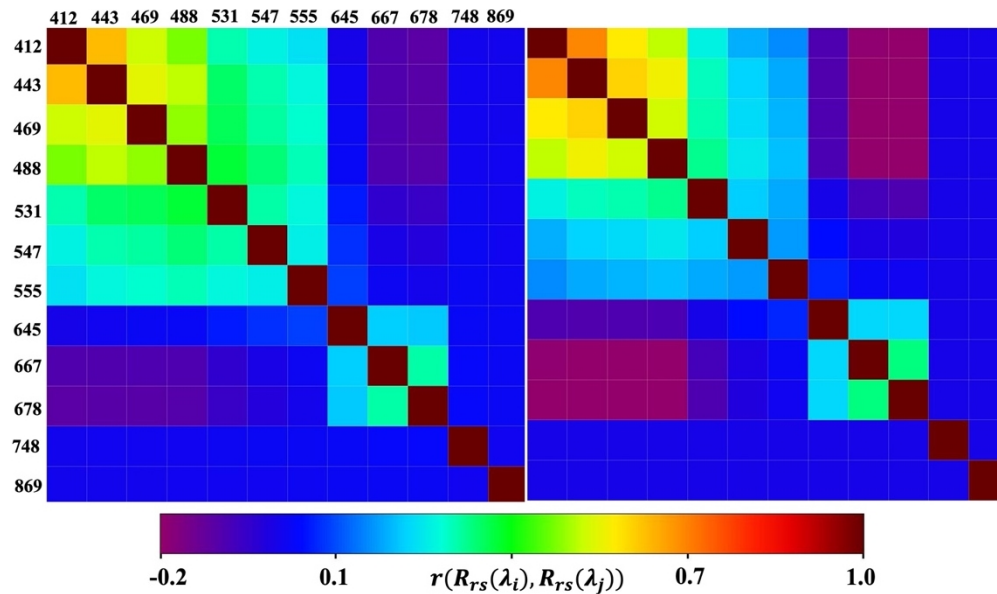


Fig. 6. $r(R_{rs}(\lambda_i), R_{rs}(\lambda_j))$ over two pixels denoted by “A” (left) and “B” (right) in Fig. 3.

3.5. Global maps

Figure 8 shows one example of 8-day global error covariance in R_{rs} derived by applying the derivative method to MODIS/Aqua data from Dec. 3-10, 2019. The 8-day products do not represent the error covariance in an 8-day (Level-3) mean as they are simply the average in each bin over that period. At this level of compositing, error covariance in R_{rs} doesn't show many obvious spatial patterns, except higher at the edge than at the center of the swath. Figure 9 shows $\delta(\text{chl}_a)$ calculated with and without error covariance in R_{rs} as well as the difference of these two. In open ocean waters, $\delta(\text{chl}_a)$ is relatively higher in the edge of swath due to the high uncertainty in R_{rs} . The much lower $\delta(\text{chl}_a)$ in some coastal waters (e.g., East Asia, Australia) results from high chl_a . Higher $\delta(\text{chl}_a)$ is found in east Mediterranean Sea, Arabian sea, and Sea of Japan.

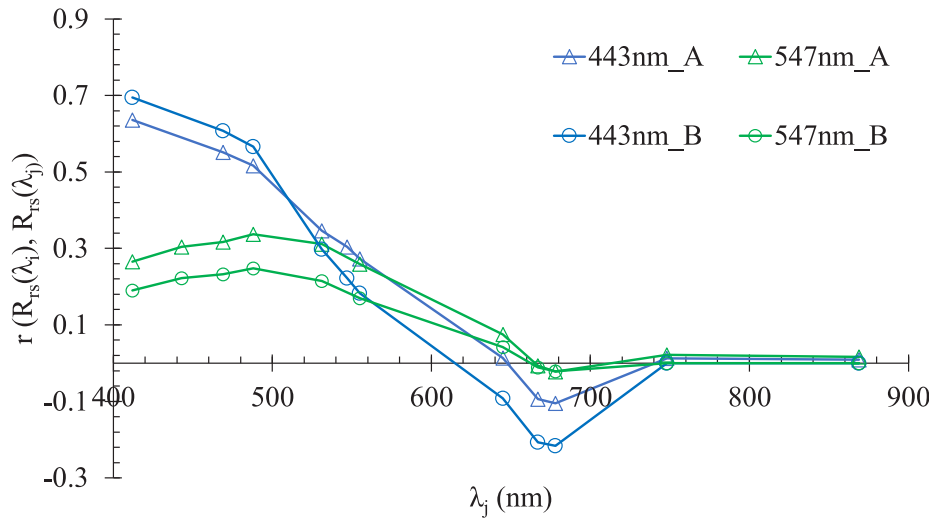


Fig. 7. Spectral $r(R_{rs}(443), R_{rs}(\lambda_j))$ and $r(R_{rs}(547), R_{rs}(\lambda_j))$ over pixels denoted by “A” and “B” in Fig. 3. Self-correlations which equal to 1 are dropped for better plot visibility.

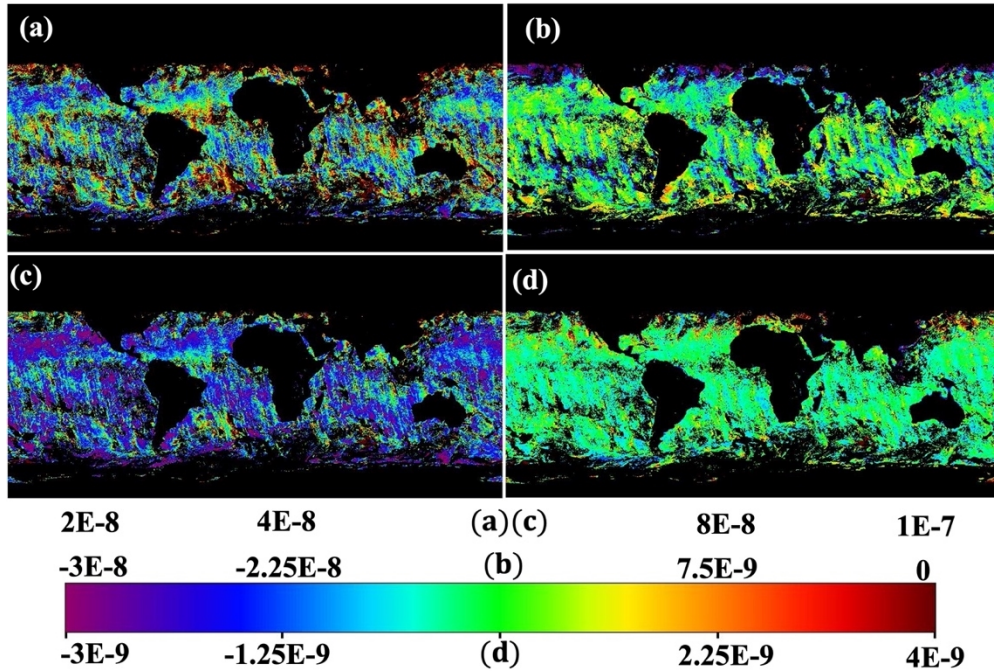


Fig. 8. 8-day (a) $u(R_{rs}(443), R_{rs}(547))$, (b) $u(R_{rs}(443), R_{rs}(667))$, (c) $u(R_{rs}(488), R_{rs}(547))$, (d) $u(R_{rs}(547), R_{rs}(667))$ calculated from the derivative method using MODIS data from Dec. 3-10, 2019.

While error covariance in R_{rs} reduces $\delta(chl_a)$ by $\sim 3.5\%$ on average (Fig. 9(d)), it is bigger in high altitude region and coastal waters than other regions. Figure 10 shows the cumulative distribution function (CDF) of $\delta(chl_a)$ over clear water pixels ($chl_a \leq 0.1 \text{ mg/m}^3$) with valid data in Fig. 9. Around 28.4% and 95.7% of clear water pixels have $\delta(chl_a) < 20\%$ and 25% respectively. But

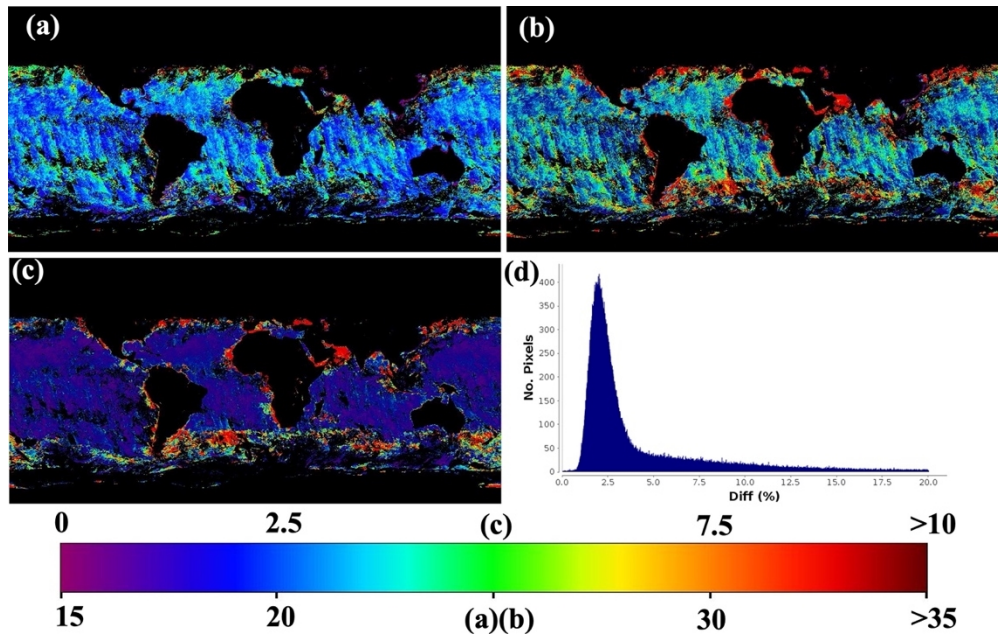


Fig. 9. 8-day $\delta(\text{chl}_a)$ calculated using R_{rs} retrieved from MODIS data from Dec. 3-10, 2019. (a) $\delta(\text{chl}_a)$ calculated by including error covariance in R_{rs} (b) $\delta(\text{chl}_a)$ calculated without error covariance in R_{rs} . (c) The difference derived by subtracting (a) from (b). (d) PDF of the difference in (c).

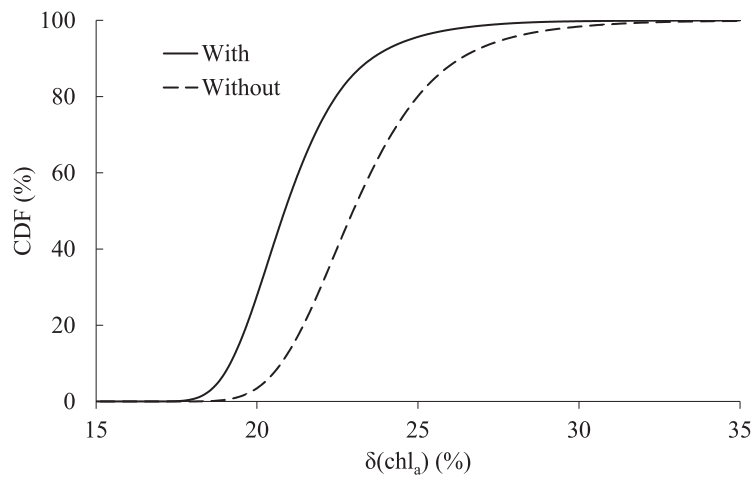


Fig. 10. Cumulative distribution function (CDF) of $\delta(\text{chl}_a)$ for all the pixels with valid data and with $\text{chl}_a \leq 0.1 \text{ mg/m}^3$ in Fig. 9. Here “with” and “without” mean $\delta(\text{chl}_a)$ calculated with and without error covariance in R_{rs} .

without error covariance in R_{rs} , those numbers decrease to 3.8% and 80.7% for $\delta(\text{chl}_a) < 20\%$ and 25% respectively. This suggests that the goal of 35% for $\delta(\text{chl}_a)$ can be achieved over deep ocean waters with the assumption of a model fitting uncertainty of 13%.

4. Conclusions

A derivative-based approach was established by [5] to calculate the uncertainty in R_{rs} retrieved from NASA's MSEPS atmospheric correction algorithm. This study extends the approach to calculate the spectral error covariance in R_{rs} . Quantification of this spectral covariance is necessary to accurately calculate the uncertainty in a host of bio-optical and biogeochemical properties of the water column that rely on spectral R_{rs} , because the band-to-band correlations are not negligible. The error covariance in R_{rs} obtained by our derivative method is found to compare reasonably well with that derived from Monte Carlo analysis, with the median ratio of the former to the latter about 0.87 for the error covariance between R_{rs} at 443 and 547 nm and about 1.10 between R_{rs} at 443 and 667 nm. This indicates the reliability of the derivative-based approach established to propagate uncertainty sources including instrument random noise, systematic uncertainty, and forward model uncertainty into R_{rs} . We also utilize the spectral error covariance in R_{rs} to calculate uncertainty in chl_a and $K_d(490)$. Compared to assuming no spectral correlation in R_{rs} uncertainty, accounting for correlation reduces the relative uncertainty in chl_a by ~1-2% in waters with $chl_a < 0.25 \text{ mg/m}^3$ and by ~5-10% in waters with $chl_a > 0.35 \text{ mg/m}^3$, with reduction >30% in some regions. Similarly, the reduction for $K_d(490)$ is typically ~2%, but it can be >20% in some regions. We further evaluate the error covariance using the results derived from evaluation of MODIS retrieved chl_a against chl_a calculated from in situ R_{rs} at MOBY, which also clearly demonstrates the ability of our approach to distinguish relatively low-uncertainty cases from high-uncertainty cases.

While the above analyses indicate that the derivative-based approach can provide reasonable spectral error covariance in R_{rs} , there are some limitations. Some other uncertainty sources (e.g., structured errors) could be relevant, and some assumptions should be updated as our knowledge improves. Examples include the correlation between uncertainty in TOA reflectance; the absolute calibration uncertainty of the 869 nm reference band; and the uncertainty in ancillary data. Despite these limitations, the approach makes significant progress towards providing useful pixel-level error covariance in R_{rs} . While demonstrated using MODIS data, it can be adapted to all the other ocean color missions processed and distributed by NASA. One practical question is how to include the error covariance matrix in R_{rs} products without increasing data file sizes by an order of magnitude or more; options may include calculating spectral correlation in the error covariance or parameterizing error covariance as a function of aerosol, chl_a and geometry. This issue will need to be addressed as it becomes more pertinent as we move forward to hyperspectral sensors with hundreds of bands such as Ocean Color Instrument (OCI) on NASA's upcoming Plankton, Aerosol, Cloud, ocean Ecosystem mission (PACE) [40].

Funding. National Aeronautics and Space Administration (PACE project, Terra and Aqua Senior Review for MODIS).

Disclosures. The authors declare no conflicts of interest.

Data availability. Data underlying the results presented in this paper are not publicly available at this time but may be obtained from the authors upon reasonable request.

References

1. M. J. Behrenfeld, J. T. Randerson, C. R. McClain, *et al.*, "Biospheric Primary Production During an ENSO Transition," *Science* **291**(5513), 2594–2597 (2001).
2. B. B. Cael, K. Bisson, E. Boss, *et al.*, "Global climate-change trends detected in indicators of ocean ecology," *Nature* **619**(7970), 551–554 (2023).
3. N. Fox, "A guide to expression of uncertainty of measurements," (GEO, 2010), https://qa4eo.org/docs/QA4EO-QAEO-GEN-DQK-006_v4.0.pdf. Accessed 1 Oct. 2023.
4. IOCCG, *Uncertainties in Ocean Colour Remote Sensing*, (International Ocean Colour Coordinating Group, Dartmouth, Canada, 2019).
5. M. Zhang, A. Ibrahim, B. A. Franz, *et al.*, "Estimating pixel-level uncertainty in ocean color retrievals from MODIS," *Opt. Express* **30**(17), 31415–31438 (2022).
6. E. Pachniak, Y. Fan, W. Li, *et al.*, "Quantifying Uncertainties in OC-SMART Ocean Color Retrievals: A Bayesian Inversion Algorithm," *Algorithms* **16**(6), 301 (2023).

7. T. Schroeder, M. Schaale, J. Lovell, *et al.*, “An ensemble neural network atmospheric correction for Sentinel-3 OLCI over coastal waters providing inherent model uncertainty estimation and sensor noise propagation,” *Remote Sens. Environ.* **270**, 112848 (2022).
8. T. Jackson, S. Sathyendranath, and F. Mélin, “An improved optical classification scheme for the Ocean Colour Essential Climate Variable and its applications,” *Remote Sens. Environ.* **203**, 152–161 (2017).
9. F. Mélin, G. Sclep, T. Jackson, *et al.*, “Uncertainty estimates of remote sensing reflectance derived from comparison of ocean color satellite data sets,” *Remote Sens. Environ.* **177**, 107–124 (2016).
10. C. Hu, L. Feng, and Z. Lee, “Uncertainties of SeaWiFS and MODIS remote sensing reflectance: Implications from clear water measurements,” *Remote Sens. Environ.* **133**, 168–182 (2013).
11. H. R. Gordon and M. Wang, “Retrieval of water-leaving radiance and aerosol optical thickness over the oceans with SeaWiFS: a preliminary algorithm,” *Appl. Opt.* **33**(3), 443–452 (1994).
12. L. I. W. McKinna, I. Cetinić, A. P. Chase, *et al.*, “Approach for Propagating Radiometric Data Uncertainties Through NASA Ocean Color Algorithms,” *Front. Earth Sci.* **7**, 176 (2019).
13. N. Lamquin, A. Mangin, C. Mazeran, *et al.*, “OLCI L2 Pixel-by-Pixel Uncertainty Propagation in OLCI Clean Water Branch,” (ESA, 2013), <https://www.eumetsat.int/media/42990>. Accessed 1 Oct. 2023.
14. D. Antoine and A. Morel, “A multiple scattering algorithm for atmospheric correction of remotely sensed ocean colour (MERIS instrument): Principle and implementation for atmospheres carrying various aerosols including absorbing ones,” *Int. J. Remote Sens.* **20**(9), 1875–1916 (1999).
15. L. Qi, Z. Lee, C. Hu, *et al.*, “Requirement of minimal signal-to-noise ratios of ocean color sensors and uncertainties of ocean color products,” *J. Geophys. Res.: Oceans* **122**(3), 2595–2611 (2017).
16. Z. Lee, R. Arnone, C. Hu, *et al.*, “Uncertainties of optical parameters and their propagations in an analytical ocean color inversion algorithm,” *Appl. Opt.* **49**(3), 369–381 (2010).
17. J. E. O’Reilly and P. J. Werdell, “Chlorophyll algorithms for ocean color sensors - OC4, OC5 & OC6,” *Remote Sens. Environ.* **229**, 32–47 (2019).
18. C. Hu, L. Feng, Z. Lee, *et al.*, “Improving Satellite Global Chlorophyll a Data Products Through Algorithm Refinement and Data Recovery,” *J. Geophys. Res.: Oceans* **124**(3), 1524–1543 (2019).
19. J. L. Muller, “SeaWiFS algorithm for the diffuse attenuation coefficient, K (490) using water-leaving radiances at 490 and 555 nm,” in *SeaWiFS Postlaunch Calibration and Validation Analyses, Part 3*, S. B. Hooker and E. R. Firestone, eds. (NASA GSFC, 2000), pp. 24–27.
20. Z. Ahmad and B. A. Franz, *Uncertainty in aerosol model characterization and its impact on ocean color retrievals*, (Goddard Space Flight Center, Maryland, 2018).
21. Z. Ahmad and B. A. Franz, “Ocean color retrieval using multiple-scattering epsilon values,” in *International Ocean Color Science Meeting 2015*, (2015).
22. NASA, “The Official NASA/OB.DAAC Data Analysis Software,” v.8.4.1, NASA (2023). <https://seadas.gsfc.nasa.gov>
23. NASA, “Ocean color,” *OB.DAAC* (2023). <https://oceancolor.gsfc.nasa.gov/>
24. D. K. Clark, H. R. Gordon, K. J. Voss, *et al.*, “Validation of atmospheric correction over the oceans,” *J. Geophys. Res.: Atmos.* **102**(D14), 17209–17217 (1997).
25. NASA, “Validation Search,” *SeaBASS* (2023). <https://seabass.gsfc.nasa.gov/search#val>
26. M. Wang, “A refinement for the Rayleigh radiance computation with variation of the atmospheric pressure,” *Int. J. Remote Sens.* **26**(24), 5651–5663 (2005).
27. H. R. Gordon and M. Wang, “Influence of oceanic whitecaps on atmospheric correction of ocean-color sensors,” *Appl. Opt.* **33**(33), 7754–7763 (1994).
28. D. Stramski and J. Piskozub, “Estimation of Scattering Error in Spectrophotometric Measurements of Light Absorption by Aquatic Particles from Three-Dimensional Radiative Transfer Simulations,” *Appl. Opt.* **42**(18), 3634–3646 (2003).
29. C. Cox and W. Munk, “Measurement of the Roughness of the Sea Surface from Photographs of the Sun’s Glitter,” *J. Opt. Soc. Am.* **44**(11), 838–850 (1954).
30. M. Wang and S. W. Bailey, “Correction of sun glint contamination on the SeaWiFS ocean and atmosphere products,” *Appl. Opt.* **40**(27), 4790–4798 (2001).
31. G. Meister, E. J. Kwiatkowska, B. A. Franz, *et al.*, “Moderate-Resolution Imaging Spectroradiometer ocean color polarization correction,” *Appl. Opt.* **44**(26), 5524–5535 (2005).
32. A. Morel, D. Antoine, and B. Gentili, “Bidirectional reflectance of oceanic waters: accounting for Raman emission and varying particle scattering phase function,” *Appl. Opt.* **41**(30), 6289–6306 (2002).
33. JCGM, “Evaluation of measurement data — Supplement 2 to the “expression of uncertainty in measurement” -Extension to any number of output quantities,” (2011).
34. S. Brown, S. Flora, M. Feinholz, *et al.*, *The marine optical buoy (MOBY) radiometric calibration and uncertainty budget for ocean color satellite sensor vicarious calibration*, SPIE Remote Sensing (SPIE, 2007), Vol. 6744.
35. A. Ibrahim, B. A. Franz, Z. Ahmad, *et al.*, “Multiband atmospheric correction algorithm for ocean color retrievals,” *Front. Earth Sci.* **7**, 116 (2019).
36. G. Zibordi, M. Talone, and F. Mélin, “Uncertainty estimate of satellite-derived normalized water-leaving radiance,” *IEEE Geosci. Remote Sensing Lett.* **19**, 1–5 (2022).
37. A. M. Sayer, Y. Govaerts, P. Kolmonen, *et al.*, “A review and framework for the evaluation of pixel-level uncertainty estimates in satellite aerosol remote sensing,” *Atmos. Meas. Tech.* **13**(2), 373–404 (2020).

38. J. Mittaz, C. J. Merchant, and E. R. Woolliams, "Applying principles of metrology to historical Earth observations from satellites," *Metrologia* **56**(3), 032002 (2019).
39. NASA, "Diffuse attenuation coefficient for downwelling irradiance at 490 nm (K_d)," *Ocean Color* (2023). <https://oceancolor.gsfc.nasa.gov/resources/atbd/kd/>
40. P. J. Werdell, M. J. Behrenfeld, P. S. Bontempi, *et al.*, "The plankton, aerosol, cloud, ocean ecosystem mission: status, science, advances," *Bull. Am. Meteorol. Soc.* **100**(9), 1775–1794 (2019).